

# Bi-Linear Modeling of Data Manifolds for Dynamic-MRI Recovery

Gaurav N. Shetty<sup>1</sup>, Konstantinos Slavakis<sup>1</sup>, Abhishek Bose<sup>2</sup>, Ukash Nakarmi<sup>3</sup>, Leslie Ying<sup>1</sup>, and Gesualdo Scutari<sup>4</sup>

<sup>1</sup>Department of Electrical Engineering, University at Buffalo, SUNY. Emails: {gauravna,kslavaki,leiying}@buffalo.edu.

<sup>2</sup>Department of Computer Science, INRIA, Université Côte d'Azur. Email: abhishek.bose@inria.fr.

<sup>3</sup>Department of Electrical Engineering and Radiology, Stanford University. Email: nakarmi@stanford.edu.

<sup>4</sup>Department of Industrial Engineering, Purdue University. Email: gscutari@purdue.edu.

**Abstract**—This paper puts forth a novel bi-linear modeling framework for data recovery via manifold-learning and sparse-approximation arguments and considers its application to dynamic magnetic-resonance imaging (dMRI). Each temporal-domain MR image is viewed as a point that lies onto or close to a smooth manifold, and landmark points are identified to describe the point cloud concisely. To facilitate computations, a dimensionality reduction module generates low-dimensional/compressed renditions of the landmark points. Recovery of the high-fidelity MRI data is realized by solving a non-convex minimization task for the linear decomposition operator and those affine combinations of landmark points which locally approximate the latent manifold geometry. An algorithm with guaranteed convergence to stationary solutions of the non-convex minimization task is also provided. The aforementioned framework exploits the underlying spatio-temporal patterns and geometry of the acquired data without any prior training on external data or information. Extensive numerical results on simulated as well as real cardiac-cine and perfusion MRI data illustrate noteworthy improvements of the advocated machine-learning framework over state-of-the-art reconstruction techniques.

**Index Terms**—Dynamic MRI, machine learning, manifold learning, low rank, sparsity, dimensionality reduction.

## I. INTRODUCTION

Magnetic-resonance imaging (MRI), a non-invasive, non-ionizing and high-fidelity visualization technology, has found widespread applications in cardiac-cine, dynamic contrast-enhanced, and neuro-imaging, playing a key role in medical research and diagnosis [1]. MRI's inherent limitations and various physiological constraints often incur slow data acquisition, while long scanning times make it an expensive process and may cause patient discomfort, thus, challenging MRI's usefulness.

Raw MRI data are observed in the  $k$ -space domain; the image (visual) data are computed by the inverse Fourier transform of the  $k$ -space ones [1]. A prominent way to speed up data acquisition is to sample the  $k$ -space or frequency domain densely enough to ensure reconstruction of a high-fidelity, artifact-free image via Fourier-transform arguments [2], [3]. In the case of dynamic (d)MRI, where an extra-temporal dimension is added to the spatial domain, sampling is also performed along the time axis. Due to MRI's slow scanning

times, it becomes difficult for the data acquisition process to keep up with the motion of the organs or the fluid flow in the field of view (FOV) [1]. It is a usual case to not be able to reach the necessary sampling density, not only in the temporal direction but also in the  $k$ -space domain, to guarantee artifact-free reconstructed images. This “under-sampling” inflicts signal aliasing and distortion [4].

Naturally, a lot of the MRI-research effort has been focusing on developing reconstruction algorithms that improve the spatio-temporal resolution of MR images given the highly under-sampled  $k$ -space data. To this end artificial-intelligence (AI) approaches have been very recently placed at the focal point of MRI research; examples are convolutional neural networks (CNNs) [5]–[7], deep variational networks (VNs) [8], and generative adversarial neural networks (GANs) [9], [10]. AI methods learn non-linear mappings via extensive offline training on large-scale datasets, different from or in addition to the acquired data, and use those learned non-linear mappings to map the observed low-resolution, or, undersampled data to their high-fidelity counterparts. In contrast to the *data-driven* AI methods, the present work, as well as the following prior-art schemes, assume *no* offline training on large-scale datasets and resort *solely* to the observed data.

A popular approach to exploit the underlying spatio-temporal patterns within dMRI data is compressed sensing (CS) [11]–[14]. Low-rank structures [15], [16] and total-variation-based schemes [17]–[19] have also been explored at length and have been found to produce promising results for slow varying dynamic data. For instance, [16] proposes the estimation, first, of a temporal basis of image time series via singular-value decomposition, prior to formulating a sparsity inducing convex-recovery task. Nevertheless, these schemes seem to be less effective when it comes to dMRI with extensive inter-frame motion or with a low number of temporal frames, as mentioned in [20], [21].

There has also been a growing interest in MRI-recovery by dictionary-learning (DL) schemes [22]–[26]. In [21], for example, the dMRI data are decomposed into two components: A low-rank one that captures the temporal (video) background, and a sparse one, described via spatio-temporal patch-based

DL, that models the (dynamic) foreground.

Manifold-learning techniques have also been employed to recover dMRI data from highly under-sampled observations [20], [27]–[29]. In [20], a graph-Laplacian matrix is formed via the Euclidean distances between points of a data cloud and is subsequently used as a regularizer in a convex-recovery task. A popular path followed by manifold-learning schemes is to perform dimensionality reduction of the collected high-dimensional data prior to applying a reconstruction algorithm, *e.g.*, [28], [29]. In the non-MRI context, [30] capitalizes, also, on a Euclidean-distance-based Laplacian matrix to perform dimensionality reduction prior to reconstructing data by local principal component analysis. In the previous schemes, *all* of the observed points participate in the dimensionality-reduction task, raising thus computational burdens, especially in cases where the number of data is excessively large. Methods that perform dimensionality reduction on properly chosen small-cardinality subsets of the observed data cloud have been introduced for clustering and classification, but *not* for regression tasks [31]–[33].

This paper follows the manifold-learning path and serves a two-fold objective: **i)** Present a machine-learning framework, the bi-linear modeling of data manifolds (BiLMDM), that contributes novelties to exploiting local and latent data structures via a sparsity-aware and bi-linear optimization task; and **ii)** apply BiLMDM to the dMRI-data recovery problem. In a nutshell, BiLMDM can be described as follows. Each vector of data, observed from a dMRI temporal frame, is modeled as a point onto or close to an unknown manifold, embedded in a Euclidean space. The only assumption imposed on the manifold is smoothness [34]. Motivated by the concept of tangent spaces of smooth manifolds, the crux of BiLMDM lies at the modeling assumption that each point of the data manifold can be approximated well by affine combinations of neighboring (*landmark*) points (*cf.* Fig. 2). Landmark points are chosen to concisely describe the observed data cloud. Similar to the dimensionality reduction modules in [29], [35], to identify any latent low-dimensional structures within the observed data and to promote an algorithmic solution with low computational footprint, low-dimensional, or, “compressed,” versions of the landmark points are computed. A *locally bi-linear* factorization model, novel for data representations, is then formed to model/fit the point cloud: One factor gathers the coefficients of the previous affine combinations of the landmark points, while the other one serves as the linear *decompression* operator that unfolds the points back to the image dimensions. Improving on our preliminary results [36], a highly modular bi-linear optimization task is tailored to the dMRI-data recovery problem, penalized by terms which account for sparsity along the temporal axis and for other modeling assumptions. A successive-convex-approximation algorithm is proposed to guarantee convergence to a stationary solutions of the previous bi-linear optimization task. BiLMDM is validated and compared with various state-of-the-art techniques via extensive tests on synthetically generated as well as real cardiac-cine and perfusion data.

The rest of the paper is organized as follows: Section II-A describes, in short, the dMRI acquisition scheme in the k-

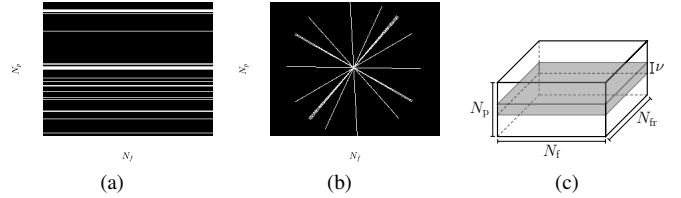


Fig. 1. (a) k-space with 1-D Cartesian sampling pattern; (b) k-space with radial sampling pattern; (c) The  $N_p \times N_f \times N_{fr}$  (k,t)-space. “Navigator (pilot) data” comprise the gray-colored  $\nu \times N_f \times N_{fr}$  area of the (k,t)-space ( $\nu \ll N_p$ ).

space domain. Section II-B details the BiLMDM’s modeling assumptions, while Sec. III describes the algorithm to solve the proposed non-convex minimization task. The extensive numerical tests of Section IV showcase that BiLMDM outperforms state-of-the-art dMRI recovery schemes. The manuscript concludes in Section V. Finally, the Appendix gathers basic mathematical facts and details that do not fit in the main body of the manuscript due to space limitations dictated by this journal.

## II. BI-LINEAR MODELING OF DATA MANIFOLDS

### A. dMRI data description

MRI data  $\mathcal{Y} \in \mathbb{C}^{N_p \times N_f}$  ( $\mathbb{C}$  denotes the set of all complex-valued numbers) are observed in *k-space* (frequency domain), which spans an area of size  $N_p \times N_f$  (*cf.* Figs. 1a and 1b), with  $N_p$  standing for the number of phase-encoding lines and  $N_f$  for the number of frequency-encoding ones [1]. Data  $\mathcal{Y}$  can be considered as the two-dimensional (discrete) Fourier transform  $\mathcal{F}(\cdot)$  of the image-domain data  $\mathcal{X} \in \mathbb{C}^{N_p \times N_f}$ , *i.e.*,  $\mathcal{Y} = \mathcal{F}(\mathcal{X})$  [1]. Without any loss of generality, this study assumes that the “low-frequency” part of  $\mathcal{Y}$  is located around the center of the  $N_p \times N_f$  area. Availability of the data over the whole k-space is infeasible in practice; the k-space is usually severely under-sampled [4]. There exist several strategies to sample the k-space; examples are the 1-D Cartesian (Fig. 1a) and the radial (Fig. 1b) ones, where the “white” lines in Figs. 1a and 1b denote the available/sampled data, while data in the “black” areas are not observed. A general trend among sampling strategies is to put more emphasis on low-frequency components, which carry contrast information and with high SNR, and select few high-frequency components, which comprise high-resolution image details. The 1-D Cartesian sampling pattern emulates the acquisition of k-space pixels via the 1-D Gaussian distribution, acquiring a large number of samples in the central k-space area while sampling few ones from the “high-frequency” area (*cf.* Fig. 1a). The radial-sampling pattern consists of radial spokes which yield dense sampling at the center of k-space, while the sampling density is decreased as one moves away from the center (*cf.* Fig. 1b).

In dMRI, an additional dimension is added to the MRI k-space to accommodate time (the axis vertical on the paper in Fig. 1c), resulting in the augmented (k,t)-space. The dMRI (k,t)-space can be viewed, in other words, as the  $N_{fr}$ -fold Cartesian product of the  $(N_p \times N_f)$ -sized MRI k-space, where  $N_{fr}$  represents the number of observed MRI frames over time. In dMRI, k-space  $\mathcal{Y}_j$  and image-domain  $\mathcal{X}_j$  data are

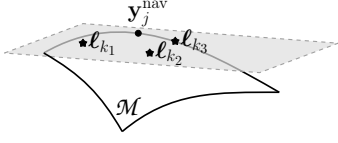


Fig. 2. Landmark points  $\{\ell_{k_i}\}_{i=1}^3$  are affinely combined to describe  $\mathbf{y}_j^{\text{nav}}$ . All affine combinations of  $\{\ell_{k_i}\}_{i=1}^3$  are depicted by the gray-colored plane.

connected via  $\mathcal{Y}_j = \mathcal{F}(\mathcal{X}_j)$ ,  $j \in \{1, \dots, N_{\text{fr}}\}$ . The (k,t) space is usually highly under-sampled. To extract reliable information from the (k,t)-space data, this work follows [20], [29] and considers a small number  $\nu$  ( $\ll N_p$ ) of phase-encoding lines (coined "navigator (pilot) data" (the gray-colored area in Fig. 1c) to learn the intrinsic low-dimensional structure of the data.

To facilitate processing, the (k,t)-space data are vectorized. More specifically,  $\text{vec}(\mathcal{Y}_j)$  stacks one column of  $\mathcal{Y}_j$  below the other to yield the complex-valued  $N_k \times 1$  vector  $\mathbf{y}_j := \text{vec}(\mathcal{Y}_j)$  where  $N_k := N_p N_{\text{fr}}$  denotes the number of pixels in every frame. To avoid notation clutter,  $\mathcal{F}$  still denotes the two-dimensional (discrete) Fourier transform even when applied to vectorized versions of image frames:  $\mathcal{F}[\text{vec}(\mathcal{X}_j)] := \text{vec}[\mathcal{F}(\mathcal{X}_j)] = \text{vec}(\mathcal{Y}_j)$ . All vectorized k-space frames are gathered in the  $N_k \times N_{\text{fr}}$  matrix  $\mathbf{Y} := [\mathbf{y}_1, \mathbf{y}_2, \dots, \mathbf{y}_{N_{\text{fr}}}]$  so that the vectorized image-domain data are  $\mathbf{X} := \mathcal{F}^{-1}(\mathbf{Y}) := [\mathcal{F}^{-1}(\mathbf{y}_1), \mathcal{F}^{-1}(\mathbf{y}_2), \dots, \mathcal{F}^{-1}(\mathbf{y}_{N_{\text{fr}}})]$ , where  $\mathcal{F}^{-1}(\cdot)$  denotes the inverse two-dimensional (discrete) Fourier transform. The navigator data of the  $j$ th k-space frame (cf. Fig. 1c),  $j \in \{1, 2, \dots, N_{\text{fr}}\}$ , are gathered into a  $\nu N_{\text{fr}} \times 1$  vector  $\mathbf{y}_j^{\text{nav}}$ . All navigator data comprise the  $\nu N_{\text{fr}} \times N_{\text{fr}}$  matrix  $\mathbf{Y}_{\text{nav}} := [\mathbf{y}_1^{\text{nav}}, \mathbf{y}_2^{\text{nav}}, \dots, \mathbf{y}_{N_{\text{fr}}}^{\text{nav}}]$ .

### B. Modeling assumptions

It is not difficult to see that  $\mathbf{Y}_{\text{nav}} = \mathbf{\Omega} \mathbf{Y}$ , where  $\mathbf{\Omega}$  is a matrix with binary entries  $\{0, 1\}$  that select entries of  $\mathbf{Y}$ . The inverse problem of recovering  $\mathbf{Y}$  from its partial  $\mathbf{Y}_{\text{nav}}$  is viable under errors, e.g., an approximation of  $\mathbf{Y}$  can be obtained via  $\mathbf{\Omega}^\dagger \mathbf{Y}_{\text{nav}}$ , where the decompressor  $\mathbf{\Omega}^\dagger$  stands for the Moore-Penrose pseudo-inverse of  $\mathbf{\Omega}$ . The following modeling hypothesis generalizes this argument.

**Assumption 1.** There exist an  $N_k \times \nu N_{\text{fr}}$  matrix  $\mathbf{G}_1$  and an  $N_k \times N_{\text{fr}}$  matrix  $\mathbf{E}_1$ , which gathers all approximation errors, such that (s.t.)  $\mathbf{Y} = \mathbf{G}_1 \mathbf{Y}_{\text{nav}} + \mathbf{E}_1$ .

A similar modeling assumption can be found in the classical principal component analysis (PCA) [37], where  $\mathbf{G}_1$  serves as the "decompression" operator (usually an orthogonal matrix) that maps the "compressed"  $\mathbf{Y}_{\text{nav}}$  back to the original data  $\mathbf{Y}$  under the approximation error  $\mathbf{E}_1$ . However, PCA identifies best-linear-fit approximations to data, which might be an inappropriate modeling assumption for several types of data [38]. The following discussion departs from PCA and establishes modeling assumptions that allow non-linear data geometries.

The high-dimensional navigator data  $\{\mathbf{y}_j^{\text{nav}}\}_{j=1}^{N_{\text{fr}}}$  carry useful information about spatio-temporal dependencies in the (k,t)-space. To promote parsimonious data representations, especially in cases where  $N_{\text{fr}}$  attains large values, it is desirable to extract a subset  $\{\ell_k\}_{k=1}^{N_\ell} \subset \{\mathbf{y}_j^{\text{nav}}\}_{j=1}^{N_{\text{fr}}}$  ( $N_\ell \leq N_{\text{fr}}$ ), called

landmark points, which provide a "concise description," in a user-defined sense, of the data cloud  $\{\mathbf{y}_j^{\text{nav}}\}_{j=1}^{N_{\text{fr}}}$ . To this end, the following assumption, often met in manifold-learning approaches [38], imposes structure on  $\{\mathbf{y}_j^{\text{nav}}\}_{j=1}^{N_{\text{fr}}}$ .

**Assumption 2.** Data  $\{\mathbf{y}_j^{\text{nav}}\}_{j=1}^{N_{\text{fr}}}$  lie on a smooth low-dimensional manifold  $\mathcal{M}$  [34] embedded in the high-dimensional Euclidean space  $\mathbb{C}^{\nu N_{\text{fr}}}$  (cf. Fig. 2).

For example, the most well-known case of a smooth manifold is a linear subspace. Based on As. 2 and the concept of the tangent space of a smooth manifold, it is conceivable that neighboring landmark points cooperate affinely to describe vector  $\mathbf{y}_j^{\text{nav}}$  (the gray-colored area in Fig. 2 depicts all possible affine combinations of  $\{\ell_{k_1}, \ell_{k_2}, \ell_{k_3}\}$ ). Upon defining the  $\nu N_{\text{fr}} \times N_\ell$  matrix  $\mathbf{\Lambda} := [\ell_1, \ell_2, \dots, \ell_{N_\ell}]$ , it is assumed that there exists an  $N_\ell \times 1$  vector  $\mathbf{b}_j$  that renders the approximation error  $\|\mathbf{y}_j^{\text{nav}} - \mathbf{\Lambda} \mathbf{b}_j\|$  small, where  $\|\cdot\|$  denotes the standard Euclidean norm of space  $\mathbb{C}^{\nu N_{\text{fr}}}$ . Since affine combinations are desirable,  $\mathbf{b}_j$  is constrained to satisfy  $\mathbf{1}_{N_\ell}^\top \mathbf{b}_j = 1$ , where  $\mathbf{1}_{N_\ell}$  stands for the all-one  $N_\ell \times 1$  vector and superscript  $\top$  denotes vector/matrix transposition. Moreover, motivated by the low-dimensional nature of  $\mathcal{M}$  (As. 2), only a few landmark points are assumed to cooperate to represent  $\mathbf{y}_j^{\text{nav}}$ , i.e.,  $\mathbf{b}_j$  is sparse. The previous arguments are summarized into the following modeling hypothesis.

**Assumption 3.** There exist a sparse  $N_\ell \times N_{\text{fr}}$  matrix  $\mathbf{B}$ , with  $\mathbf{1}_{N_\ell}^\top \mathbf{B} = \mathbf{1}_{N_{\text{fr}}}^\top$ , and a  $\nu N_{\text{fr}} \times N_{\text{fr}}$  matrix  $\mathbf{E}_2$ , which gathers approximation errors, s.t.  $\mathbf{Y}_{\text{nav}} = \mathbf{\Lambda} \mathbf{B} + \mathbf{E}_2$ .

The previous assumption holds true in the prototypical case where  $\mathcal{M}$  is a linear subspace and  $\mathbf{Y}_{\text{nav}}$  contains as columns a basis of  $\mathcal{M}$ . Any matrix which includes as columns that basis may serve as  $\mathbf{\Lambda}$ . Since the affine hull [39] of the columns of  $\mathbf{\Lambda}$  coincides with  $\mathcal{M}$ , there exists a coefficient matrix  $\mathbf{B}$  that satisfies the affine constraints  $\mathbf{1}_{N_\ell}^\top \mathbf{B} = \mathbf{1}_{N_{\text{fr}}}^\top$  and  $\mathbf{Y}_{\text{nav}} = \mathbf{\Lambda} \mathbf{B}$ .

Although several strategies may be implemented to identify the landmark points  $\mathbf{\Lambda}$ , a greedy optimization methodology, introduced in [33], is adopted here. In short, at every step of the algorithm, a landmark point is selected from  $\{\mathbf{y}_j^{\text{nav}}\}_{j=1}^{N_{\text{fr}}}$  that maximizes, over all *un-selected*  $\{\mathbf{y}_j^{\text{nav}}\}_{j=1}^{N_{\text{fr}}}$ , the minimum distance to the landmark points which have been already selected up to the previous step of the algorithm. The algorithm of [33] scores a computational complexity of order  $\mathcal{O}(N_\ell N_{\text{fr}})$ , which is naturally heavier than that of a procedure that selects  $\{\ell_k\}_{k=1}^{N_\ell}$  randomly from  $\{\mathbf{y}_j^{\text{nav}}\}_{j=1}^{N_{\text{fr}}}$ .

Still, the landmark points (columns of  $\mathbf{\Lambda}$ ) are high dimensional. To meet restrictions imposed by finite computational resources, it is desirable to reduce the dimensionality of  $\mathbf{\Lambda}$ . To this end, the methodology of [35], which is motivated by [38], [40], is employed. The approach comprises two steps.

1) Given  $\mathbf{\Lambda}$  and a user-defined  $\lambda_W > 0$ , solve

$$\begin{aligned} \min_{\mathbf{W} \in \mathbb{C}^{N_\ell \times N_\ell}} \|\mathbf{\Lambda} - \mathbf{\Lambda} \mathbf{W}\|_{\text{F}}^2 + \lambda_W \|\mathbf{W}\|_1 \\ \text{s.t. } \mathbf{1}_{N_\ell}^\top \mathbf{W} = \mathbf{1}_{N_\ell}^\top \text{ and } \text{diag}(\mathbf{W}) = \mathbf{0}, \end{aligned} \quad (1a)$$

where  $\|\cdot\|_{\text{F}}$  stands for the Frobenius norm of a matrix. Since  $\{\ell_k\}_{k=1}^{N_\ell}$  lie on the manifold  $\mathcal{M}$ , then according to As. 2 and Fig. 2, any point taken from  $\{\ell_k\}_{k=1}^{N_\ell}$  may be faithfully approximated by an affine combination of

the rest of the landmark points. In other words, there exists a matrix  $\mathbf{W}$  s.t.  $\mathbf{\Lambda} \approx \mathbf{\Lambda}\mathbf{W}$ . With  $\mathbf{1}_{N_\ell}^\top \mathbf{W} = \mathbf{1}_{N_\ell}^\top$  manifesting the previous desire for affine combinations, the constraint  $\text{diag}(\mathbf{W}) = \mathbf{0}$  is used to exclude the trivial solution of the identity matrix  $\mathbf{I}_{N_\ell}$  for  $\mathbf{W}$ . Task (1a) is an affinely constrained composite convex minimization task, and, hence, the framework of [41] can be employed to solve it, due to the flexibility by which [41] deals with affine constraints when compared with state-of-the-art convex optimization techniques.

- 2) Once  $\mathbf{W}$  is obtained from the previous step and for a user-defined integer number  $d \leq \min\{N_\ell, \nu N_f\}$ , solve

$$\min_{\check{\mathbf{\Lambda}} \in \mathbb{C}^{d \times N_\ell}} \|\check{\mathbf{\Lambda}} - \check{\mathbf{\Lambda}}\mathbf{W}\|_F^2 \text{ s.t. } \check{\mathbf{\Lambda}}\check{\mathbf{\Lambda}}^H = \mathbf{I}_d, \quad (1b)$$

where the constraint  $\check{\mathbf{\Lambda}}\check{\mathbf{\Lambda}}^H = \mathbf{I}_d$  is used to exclude the trivial solution of  $\check{\mathbf{\Lambda}} = \mathbf{0}$ , and the superscript H denotes the Hermitian transpose of a matrix. The solution of the previous task is nothing but the complex conjugate transpose of the matrix which comprises the  $d$  minimal eigenvectors of  $(\mathbf{I}_{N_\ell} - \mathbf{W})(\mathbf{I}_{N_\ell} - \mathbf{W})^H$ .

**Assumption 4.** There exist an  $N_k \times d$  matrix  $\mathbf{G}_3$  and an  $N_k \times N_\ell$  matrix  $\mathbf{E}_3$ , which gathers all approximation errors, s.t.  $\mathbf{\Lambda} = \mathbf{G}_3\check{\mathbf{\Lambda}} + \mathbf{E}_3$ .

Matrix  $\mathbf{G}_3$  can be viewed as the ‘‘decompression’’ operator which reconstructs the ‘‘full’’  $\mathbf{\Lambda}$  from its low-dimensional representation  $\check{\mathbf{\Lambda}}$ .

Putting modeling assumptions 1, 3 and 4 together, it can be verified that there exist matrices  $\mathbf{G}$  and  $\mathbf{E}$  s.t.  $\mathbf{Y} = \mathbf{G}\check{\mathbf{\Lambda}}\mathbf{B} + \mathbf{E}$ . Upon defining  $\mathbf{U} := \mathcal{F}^{-1}(\mathbf{G})$ , and since  $\mathbf{G}\check{\mathbf{\Lambda}}\mathbf{B} = \mathcal{F}(\mathbf{U}\check{\mathbf{\Lambda}}\mathbf{B}) = \mathcal{F}(\mathbf{U}\check{\mathbf{\Lambda}}\mathbf{B})$ , by virtue of the linearity of  $\mathcal{F}$ , the following bi-linear model between  $\mathbf{Y}$  and the unknowns  $(\mathbf{U}, \mathbf{B})$  is established:

$$\mathbf{Y} = \mathcal{F}(\mathbf{U}\check{\mathbf{\Lambda}}\mathbf{B}) + \mathbf{E}. \quad (2)$$

Bi-linearity means that if  $\mathbf{U}$  (or  $\mathbf{B}$ ) is fixed to a specific value, then  $\mathbf{Y}$  is linear with respect to  $\mathbf{B}$  (or  $\mathbf{U}$ ), modulo the error  $\mathbf{E}$  term. Interestingly, the linearity of  $\mathcal{F}^{-1}$  suggests that the previous modeling hypothesis holds true also in the image domain:  $\mathcal{F}^{-1}(\mathbf{Y}) = \mathbf{U}\check{\mathbf{\Lambda}}\mathbf{B} + \mathcal{F}^{-1}(\mathbf{E})$ .

### III. THE BI-LINEAR RECOVERY TASK AND ITS ALGORITHMIC SOLUTION

In practice, only few (k,t)-space data are known. To explicitly take account of the limited number of data, a (linear) sampling/masking operator  $\mathcal{S}(\cdot)$  is introduced, where  $\mathcal{S}(\mathbf{Y})$  leaves the entries of  $\mathbf{Y}$  as they are at sampled or observed positions of the k-space domain while nullifying all the rest. The sampling operator is capable of mimicking any sampling strategy, such as Cartesian, radial, spiral, *etc.* It is also often in dMRI that image frames capture a periodic process, *e.g.*, heart movement, other than the static background. In other words, it is reasonable to assume that in (2), the one-dimensional Fourier transform  $\mathcal{F}_t$  of the  $1 \times N_{fr}$  time profile of every one of the  $N_k$  pixels, *i.e.*, every row of the matrix  $\mathcal{F}_t(\mathbf{U}\check{\mathbf{\Lambda}}\mathbf{B})$ , is a sparse vector.

#### Algorithm 1 Recovering the dMRI data

**Input:** Available are data  $\mathcal{S}(\mathbf{Y})$ , including the navigator  $\mathbf{Y}_{nav}$  ones. Choose parameters  $\lambda_1, \lambda_2, \lambda_3, C_U, \tau_U, \tau_B > 0$ , as well as  $\zeta \in (0, 1)$  and  $\gamma_0 \in (0, 1]$ .

**Output:** Extract the limit points  $\mathbf{U}_*$  and  $\mathbf{B}_*$  of sequences  $(\mathbf{U}_n)_n$  and  $(\mathbf{B}_n)_n$ , respectively, and recover the dMRI data by the estimate  $\hat{\mathbf{X}} := \mathbf{U}_*\check{\mathbf{\Lambda}}\mathbf{B}_*$ .

- 1: Identify landmark points  $\mathbf{\Lambda}$  from the columns of  $\mathbf{Y}_{nav}$  according to [33] (*cf.* Sec. II-B).
- 2: Compute the ‘‘compressed’’  $\check{\mathbf{\Lambda}}$  according to (1).
- 3: Arbitrarily fix  $(\mathbf{U}_0, \mathbf{B}_0, \mathbf{Z}_0)$  and set  $n = 0$ .
- 4: **while**  $n \geq 0$  **do**
- 5: Available are  $(\mathbf{U}_n, \mathbf{B}_n, \mathbf{Z}_n)$  and  $\gamma_n$ .
- 6: Let  $\gamma_{n+1} := \gamma_n(1 - \zeta\gamma_n)$ .
- 7: Obtain  $\hat{\mathbf{U}}_n$  of (4a) and  $\hat{\mathbf{B}}_n$  of (4b) via Alg. 2, and the  $(i, j)$ th entry of  $\hat{\mathbf{Z}}_n, \forall (i, j)$ , via the following soft-thresholding rule:
$$[\hat{\mathbf{Z}}_n]_{ij} := [\mathcal{F}_t(\mathbf{U}_n\check{\mathbf{\Lambda}}\mathbf{B}_n)]_{ij} \cdot \left( 1 - \frac{\lambda_2/\lambda_1}{\max\{\lambda_2/\lambda_1, |[\mathcal{F}_t(\mathbf{U}_n\check{\mathbf{\Lambda}}\mathbf{B}_n)]_{ij}|\}} \right).$$
- 8: Update
$$(\mathbf{U}_{n+1}, \mathbf{B}_{n+1}, \mathbf{Z}_{n+1}) := (1 - \gamma_{n+1})(\mathbf{U}_n, \mathbf{B}_n, \mathbf{Z}_n) + \gamma_{n+1}(\hat{\mathbf{U}}_n, \hat{\mathbf{B}}_n, \hat{\mathbf{Z}}_n).$$
- 9: Set  $n$  equal to  $n + 1$  and go to step 4.
- 10: **end while**

All of the previous modeling assumptions are incorporated in the following recovery task: Given the positive real-valued parameters  $\lambda_1, \lambda_2, \lambda_3, C_U$ , solve

$$\begin{aligned} \min_{(\mathbf{U}, \mathbf{B}, \mathbf{Z})} & \underbrace{\frac{1}{2} \|\mathcal{S}(\mathbf{Y}) - \mathcal{S}\mathcal{F}(\mathbf{U}\check{\mathbf{\Lambda}}\mathbf{B})\|_F^2}_{T1} + \underbrace{\frac{\lambda_1}{2} \|\mathbf{Z} - \mathcal{F}_t(\mathbf{U}\check{\mathbf{\Lambda}}\mathbf{B})\|_F^2}_{T2} \\ & + \underbrace{\lambda_2 \|\mathbf{Z}\|_1}_{T3} + \underbrace{\lambda_3 \|\mathbf{B}\|_1}_{T4} \\ \text{s.t. } & \underbrace{\|\mathbf{U}\mathbf{e}_i\| \leq C_U, \forall i \in \{1, \dots, d\}}_{C1}; \quad \underbrace{\mathbf{1}_{N_\ell}^\top \mathbf{B} = \mathbf{1}_{N_{fr}}^\top}_{C2}; \\ & \mathbf{U} \in \mathbb{C}^{N_k \times d}; \mathbf{B} \in \mathbb{C}^{N_\ell \times N_{fr}}; \mathbf{Z} \in \mathbb{C}^{N_k \times N_{fr}}, \end{aligned} \quad (3)$$

where  $\mathbf{e}_i$  denotes the  $i$ th column of the identity matrix  $\mathbf{I}_d$ . Elaborating more on the recovery task (3), T1 corresponds to the data-fit term, while T2 and T3 introduce the auxiliary variable  $\mathbf{Z}$ , used to impose a sparsity constraint on  $\mathcal{F}_t(\mathbf{U}\check{\mathbf{\Lambda}}\mathbf{B})$ . T4 imposes a sparsity constraint on  $\mathbf{B}$ , following the discussion on As. 3. Bound  $C_U$  in C1 is used to prevent unbounded solutions for  $\mathbf{U}$  due to the scaling ambiguity in the bi-linear term  $\mathbf{U}\check{\mathbf{\Lambda}}\mathbf{B}$ . C2 adds the affine constraint discussed in As. 3.

The successive-convex-approximation framework of [42] is employed to solve (3) and is presented in a concise form in steps 4–10 of Alg. 1. Convergence to a stationary solution of (3) is guaranteed [42]. Step 7 of Alg. 1 comprises convex minimization sub-tasks. More specifically, at every step of the algorithm, given  $(\mathbf{U}_n, \mathbf{B}_n, \mathbf{Z}_n)$ , the following estimates are

---

**Algorithm 2** Computing  $\hat{\mathbf{U}}_n$  of (4a) and  $\hat{\mathbf{B}}_n$  of (4b)

---

**Input:**  $\mathbf{D}$  is either  $\mathbf{U}_n$  or  $\mathbf{B}_n$  in step 4 of Alg. 1. Choose parameter  $\alpha \in [0.5, 1)$ .

**Output:**  $\hat{\mathbf{U}}_n$  and  $\hat{\mathbf{B}}_n$  are set equal to the limit  $\mathbf{H}_*$  of the sequence  $(\mathbf{H}_k)_k$ .

- 1: Compute the Lipschitz coefficient  $L$  via (12) or (19), and choose  $\lambda \in (0, 2(1 - \alpha)/L)$ .
- 2:  $\mathbf{H}_0 := \mathbf{D}$ .
- 3: Letting  $T$  be either (14) or (21), define  $T_\alpha := \alpha T + (1 - \alpha)\text{Id}$ , where  $\text{Id}$  denotes the identity operator.
- 4: Set  $\mathbf{H}_{1/2} := T_\alpha(\mathbf{H}_0) - \lambda \nabla g_1(\mathbf{H}_0)$ , where the gradient  $\nabla g_1(\mathbf{H}_0)$  takes the form of either (10) or (18).
- 5: Set  $\mathbf{H}_1 := \text{Prox}_{\lambda g_2}(\mathbf{H}_{1/2})$ , where the proximal operator takes the form of either (13) or (20).
- 6: **while**  $k \geq 0$  **do**
- 7:  $\mathbf{H}_{k+3/2} := \mathbf{H}_{k+1/2} + T(\mathbf{H}_{k+1}) - \lambda \nabla g_1(\mathbf{H}_{k+1}) - T_\alpha(\mathbf{H}_k) + \lambda \nabla g_1(\mathbf{H}_k)$ .
- 8:  $\mathbf{H}_{k+2} := \text{Prox}_{\lambda g_2}(\mathbf{H}_{k+3/2})$ .
- 9: Set  $k$  equal to  $k + 1$  and go to step 6.

10: **end while**

---

required (for  $\tau_U, \tau_B > 0$ ):

$$\begin{aligned} \hat{\mathbf{U}}_n \in \arg \min_{\mathbf{U}} \frac{1}{2} \|\mathcal{S}(\mathbf{Y}) - \mathcal{S}\mathcal{F}(\mathbf{U}\check{\mathbf{A}}\mathbf{B}_n)\|_{\mathbb{F}}^2 + \frac{\tau_U}{2} \|\mathbf{U} - \mathbf{U}_n\|_{\mathbb{F}}^2 \\ + \frac{\lambda_1}{2} \|\mathbf{Z}_n - \mathcal{F}_t(\mathbf{U}\check{\mathbf{A}}\mathbf{B}_n)\|_{\mathbb{F}}^2 \\ \text{s.to } \|\mathbf{U}\mathbf{e}_i\| \leq C_U, \forall i \in \{1, \dots, d\}. \end{aligned} \quad (4a)$$

$$\begin{aligned} \hat{\mathbf{B}}_n \in \arg \min_{\mathbf{B}} \frac{1}{2} \|\mathcal{S}(\mathbf{Y}) - \mathcal{S}\mathcal{F}(\mathbf{U}_n\check{\mathbf{A}}\mathbf{B})\|_{\mathbb{F}}^2 + \frac{\tau_B}{2} \|\mathbf{B} - \mathbf{B}_n\|_{\mathbb{F}}^2 \\ + \frac{\lambda_1}{2} \|\mathbf{Z}_n - \mathcal{F}_t(\mathbf{U}_n\check{\mathbf{A}}\mathbf{B})\|_{\mathbb{F}}^2 + \lambda_3 \|\mathbf{B}\|_1 \\ \text{s.to } \mathbf{1}_{N_\ell}^T \mathbf{B} = \mathbf{1}_{N_{\text{fr}}}^T. \end{aligned} \quad (4b)$$

Both tasks in (4) can be viewed as affinely constrained composite convex minimization tasks, hence allowing the use of [41], as described in Alg. 2. From a computational complexity perspective, it is worth pointing out that the proposed scheme relies on minimization sub-tasks, and computational complexities depend thus on the solver adopted for solving those sub-tasks. Here, [41] employs only first-order information (gradients) and proximal mappings, *e.g.*, soft-thresholding rules and projection mappings. The implementation of [41] for the specific tasks (4) is presented in Alg. 2, and details are deferred to the supplementary file of this manuscript. Notice also that the previous minimization sub-tasks can be solved in parallel. Furthermore, problems 4 can be solved inexactly at each iteration (with increasing precision, as described in [42]), which contributes to reducing the computation cost of each iteration; we refer to [42] for more details.

#### IV. NUMERICAL RESULTS

The proposed framework is tested and validated on three datasets, used also in [15], [16], [27], [29], [43]: **i)** Magnetic-resonance extended cardiac-torso (MRXCAT) cine phantom [44]; **ii)** a physiologically-improved nonuniform cardiac torso (PINCAT) phantom [43]; and **iii)** cardiac phantom generated from real MR scans [16]. All experiments were conducted

on a 12-core Intel(R) 2.40 GHz Linux-based system with 48GB RAM, with implementations realized in MATLAB [45]. The proposed method is compared with the following state-of-the-art methods: Partially separable sparsity aware model (PS-Sparse) [16], joint manifold learning and sparsity aware (MLS) framework [29], smoothness regularization on manifolds (SToRM) [20] and low rank and adaptive sparse signal model (LASSI) [21]. The publicly available MATLAB implementations of SToRM [46] and LASSI [47] were employed. MATLAB code was also written to realize the algorithmic solutions of [41] to the convex-optimization problems posed in PS-Sparse and MLS. Parameters were tuned to produce the least NRMSE for each algorithm at each sampling ratio and on every dataset. Optimized and time-efficient C/C++ versions of the developed MATLAB code for BiLMDM are not considered in this work.

Quality of reconstruction is evaluated by the normalized-root-mean-square error (NRMSE), defined as

$$\text{NRMSE} := \frac{\|\mathbf{X} - \hat{\mathbf{X}}\|_{\mathbb{F}}}{\|\mathbf{X}\|_{\mathbb{F}}}, \quad (5)$$

where  $\mathbf{X}$  represents the fully sampled, high-fidelity and original image-domain data, while  $\hat{\mathbf{X}}$  represents an estimate of  $\mathbf{X}$  computed by the reconstruction schemes. The proposed framework is validated over a range of sampling/acceleration rates, defined by  $N_k N_{\text{fr}} / (\# \text{ of acquired voxels})$ . 1-D Cartesian (Fig. 1a) as well as radial (Fig. 1b) sampling were applied to all of the datasets. To save space, only the 1-D Cartesian-sampling results are demonstrated for the MRXCAT dataset, while radial-sampling ones are shown for the PINCAT and the real-MR datasets. Nevertheless, similar results to the ones exhibited here hold also for the sampling strategies not included in the manuscript for all employed algorithms.

##### A. MRXCAT phantom

The extended cardiac torso (XCAT) framework was used to generate the MRXCAT phantom [44]; a breath-hold cardiac cine data of spatial size  $(N_p, N_f) = (408, 408)$  corresponding to a spatial resolution of  $1.56 \times 1.56 \text{ mm}^2$  for a FOV of  $400 \times 400 \text{ mm}^2$ . The cardiac cine phantom generated is spread across  $N_{\text{fr}} = 360$  time frames in the temporal direction, consisting of 15 cardiac cycles and 24 cardiac phases. The MRXCAT-phantom dataset is characterized by its limited inter-frame variations and periodic nature along the temporal direction, unlike the other two datasets.

Fig. 3a provides quantitative comparisons for a range of acceleration factors, while qualitative analyses are shown in Figs. 5 and 6. On the quantitative front, Fig. 4a provides the fluctuations in the NRMSE across the time frames. It is evident from Fig. 3a that the proposed BiLMDM consistently outperforms the state-of-the-art schemes over the entire range of acceleration rates. It is worth noticing here that BiLMDM scores similar NRMSE values to PS-Sparse and MLS, at specific acceleration rates, even though it uses a small subset of the navigator data (landmark points) in this case  $N_\ell = 50$ ,  $d = 4$ , in contrast to PS-Sparse and MLS that utilize the whole set of navigator data. BiLMDM's performance is consistent for every frame in the time series as displayed in

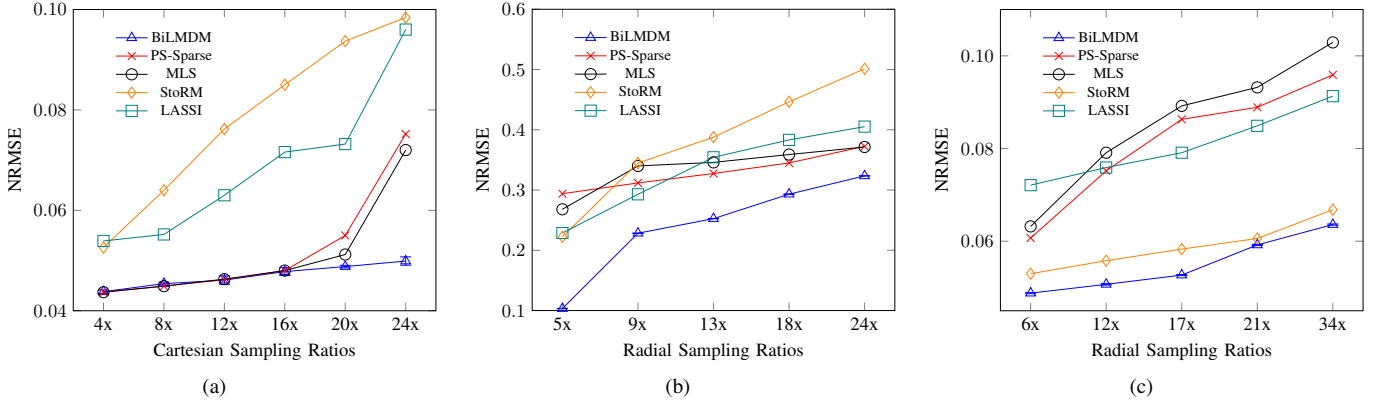


Fig. 3. NRMSE values [cf. (5)] computed for (a) MRXCAT cardiac cine data, (b) aperiodic PINCAT data, and (c) real cardiac cine data vs. acceleration/sampling rates. The NRMSE plot for BiLMDM, given the non-convex nature of the recovery task, is averaged over 25 independent trials, with different initialization points for each trial. Error bars are also used to indicate the deviation from the sample means due to the random initializations of the non-convex algorithmic scheme. There are points where the error bars are too small to be clearly visible.

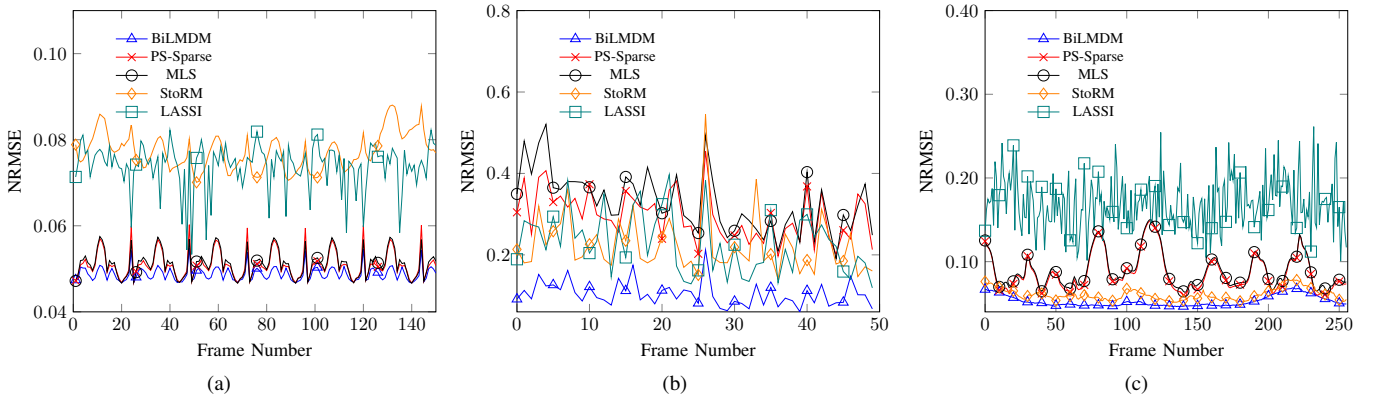


Fig. 4. Framewise-NRMSE values for (a) MRXCAT cardiac cine data (acceleration rate: 12x), (b) aperiodic PINCAT data (acceleration rate: 5x), and (c) real cardiac cine data (acceleration rate: 17x) for PS-Sparse [(a)  $0.054 \pm 3 \times 10^{-3}$  (b)  $0.2939 \pm 6.1 \times 10^{-2}$  (c)  $0.0863 \pm 2.1 \times 10^{-2}$ ], MLS [(a)  $0.051 \pm 3.1 \times 10^{-3}$  (b)  $0.268 \pm 7.4 \times 10^{-2}$  (c)  $0.0892 \pm 2 \times 10^{-2}$ ], StoRM [(a)  $0.0844 \pm 2.6 \times 10^{-2}$  (b)  $0.2224 \pm 7.2 \times 10^{-2}$  (c)  $0.0583 \pm 6.6 \times 10^{-3}$ ], LASSI [(a)  $0.0732 \pm 6 \times 10^{-3}$  (b)  $0.2133 \pm 4.6 \times 10^{-2}$  (c)  $0.0791 \pm 3.1 \times 10^{-2}$ ] and BiLMDM [(a)  $0.0488 \pm 1.6 \times 10^{-3}$ , (b)  $0.1033 \pm 3 \times 10^{-2}$ , (c)  $0.0527 \pm 6.4 \times 10^{-3}$ ]. The previous numerical values demonstrate the (sample mean over all  $N_{fr}$  frames)  $\pm$  (standard deviation from the sample mean). Consistent with simulation results, BiLMDM exhibits less fluctuations in error across all the frames over the rest of the methods.

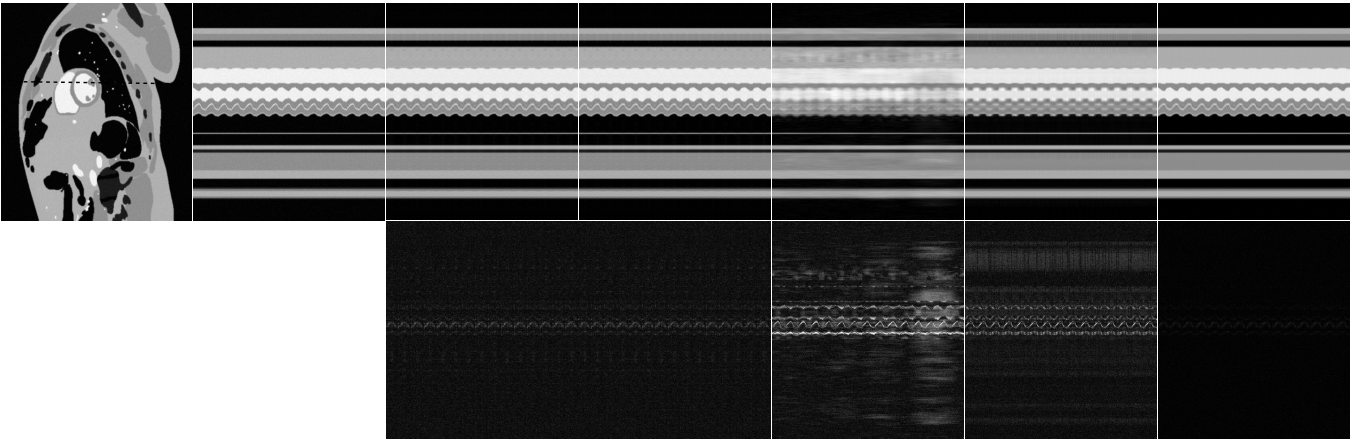


Fig. 5. Temporal cross-sections for MRXCAT cardiac cine (acceleration rate: 20x). Left to right: Gold standard (spatial frame), gold standard (temporal cross-section), PS-Sparse (0.055), MLS (0.0512), SToRM (0.0844), LASSI (0.0732) and BiLMDM ( $0.0488 \pm 2.5 \times 10^{-4}$ ). The previous numerical values indicate the NRMSE for the complete dataset, in addition to the standard deviation (for BiLMDM only) obtained after running the non-convex algorithmic scheme for 25 independent trials. Top to bottom: Temporal cross section and error maps. The temporal location of the frames is indicated by the dotted line in the gold-standard (spatial-frame) image.

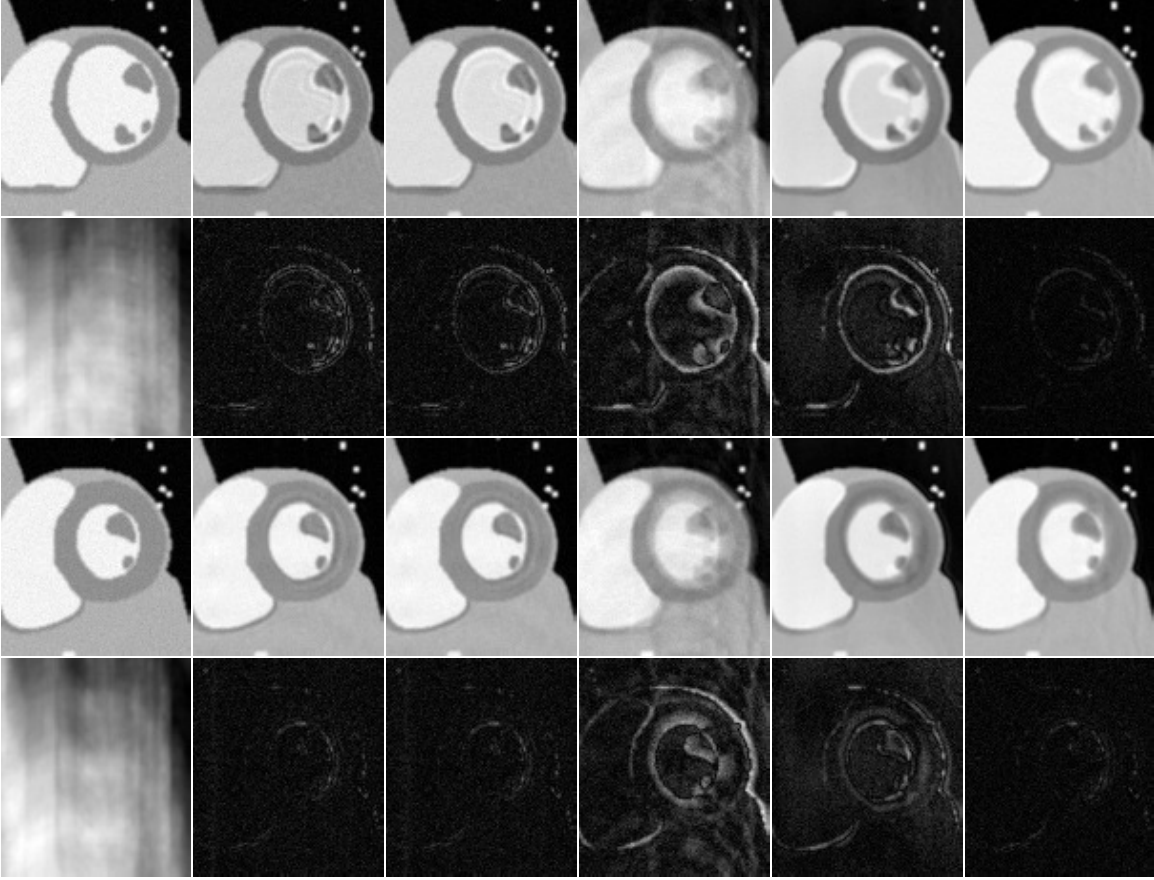


Fig. 6. Spatial results for MRXCAT cardiac cine (acceleration rate: 20x). Left to right: Gold standard, PS-Sparse (0.055), MLS (0.0512), SToRM (0.0844), LASSI (0.0732) and BiLMDM ( $0.0488 \pm 2.5 \times 10^{-4}$ ). The previous numerical values indicate the NRMSE for the complete dataset, in addition to the standard deviation (for BiLMDM only) obtained after running the non-convex algorithmic scheme for 25 independent trials. Top to bottom: Diastole phase (frame 1 of the time series), the under-sampled image followed by error maps, systole phase (frame 12 of the time series) and the under-sampled image followed by error maps.

Fig. 4a, and exhibits the least NRMSE and least NRMSE deviation for every frame, unlike LASSI and SToRM.

Fig. 6 focuses on a dynamic region of interest (ROI) from the end-diastolic and end-systolic phases. The proposed framework exhibits reconstruction of a high-resolution image with contrast close to the gold standard, as opposed to the alias-infected reconstruction of SToRM or the noisy reconstructions of PS-Sparse, MLS and LASSI. The error maps in Figs. 5 and 6 provide visual proof of the improvements in reconstruction. BiLMDM shows significant improvements at the image edges, as visualized in the error maps for both the diastolic and systolic phases. Moreover, PS-Sparse, MLS and LASSI exhibit faint-right artifacts, unlike BiLMDM. The temporal cross sections in Fig. 5 are consistent with the spatial results in Fig. 6.

### B. PINCAT phantom data

The PINCAT phantom made available by [15], [43], [48] (see [49] for the link to the data) emulates the cardiac perfusion dynamics and accounts for extreme contrast variations in the right and left ventricle regions of the heart. It is assumed that the data is acquired using a single coil of maximum sensitivity

over the FOV containing the heart. The phantom data consists of an image with the spatial size  $(N_p, N_f) = (128, 128)$ , corresponding to a spatial resolution of  $1.5 \times 1.5 \text{ mm}^2$  and spreading across  $N_{fr} = 50$  frames in the temporal direction. Unlike MRXCAT, PINCAT dataset is aperiodic in nature with very few temporal frames. The results, as shown in Fig. 3b, indicate NRMSE values which range from 0.1 to 0.32 for acceleration rates that range from 5x to 24x for  $N_\ell = 40$ ,  $d = 15$ . Even though the NRMSE values are higher in comparison to the MRXCAT ones, BiLMDM significantly outperforms the other reconstruction schemes.

Qualitative results are also exhibited in Fig. 7 and 8 for the PINCAT dataset. BiLMDM recovers MR images with almost the same contrast as the gold standard, whereas PS-Sparse and MLS fail to match the desired contrast (*cf.* the corresponding error maps). BiLMDM also exhibits the minimum aliasing effect in comparison to SToRM and LASSI. Although BiLMDM lacks subjectively in the resolution of the reconstructed image, it is still better in comparison with the competing schemes. The temporal cross sections give a better insight into the dynamics of the reconstructed dynamic MR images in Fig. 8. While significant motion blurring and noise is observed for the images reconstructed by PS-Sparse and MLS, and grainy

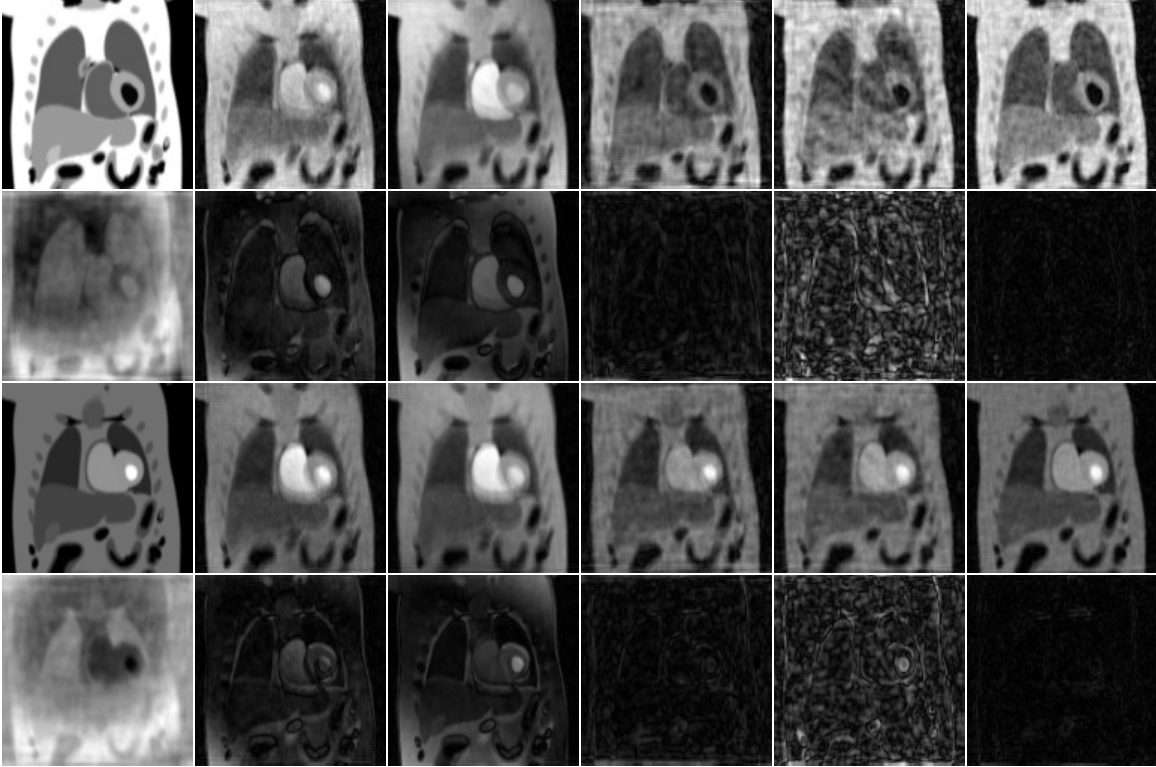


Fig. 7. Spatial results for PINCAT phantom (acceleration rate: 5x). Left to right: Gold standard, PS-Sparse (0.2939), MLS (0.268), SToRM (0.2224), LASSI (0.2287) and BiLMDM ( $0.1033 \pm 3.1 \times 10^{-4}$ ). The previous numerical values indicate the NRMSE for the complete dataset, in addition to the standard deviation (for BiLMDM only) obtained after running the non-convex algorithmic scheme for 25 independent trials. Top to bottom: Diastole phase (frame 5 of the time series), the under-sampled image followed by error maps, systole phase (frame 28 of the time series) and the under-sampled image followed by error maps.

artifacts for SToRM and LASSI, the error maps of BiLMDM demonstrate fewer artifacts and blurring along the temporal direction. The resolution defects may be mainly attributed to the low number of temporal frames and the aperiodic nature of the data along the time axis.

### C. Cardiac phantom generated from real MR scan

Besides synthetically generated MR images, real human-cardiac cine MR data were also acquired [16] with the following parameters: spatial size  $(N_p, N_f) = (200, 256)$ , FOV =  $273 \times 350 \text{ mm}^2$ , resulting in a spatial resolution of  $1.36 \times 1.36 \text{ mm}^2$ . The data were acquired during a single breath hold. Multiple time-wraps (introducing temporal variations) and quasi-periodic spatial deformation [50] (to model respiration) were then used to generate a temporal sequence with  $N_{fr} = 256$  frames. The results in Fig. 3c, similar to those on the previous two datasets, show that BiLMDM outperforms the rest of the techniques with NRMSE values ranging from 0.05 to 0.061 for  $N_\ell = 35$ ,  $d = 12$ .

With regards to Figs. 9 and 10, significant blurring and deformations can be observed for PS-Sparse, MLS and LASSI, in contrast to the sharper images produced by BiLMDM for both the end-diastolic and end-systolic phases. There are slight improvements over SToRM, which are illustrated via the error maps. At the same time, it is worth noting that in the end-systolic phase, PS-Sparse, MLS and LASSI produce an

enlargement (deformation) of a certain area of the image. The temporal cross sections in Fig. 9 indicate significant motion blurring for PS-Sparse, MLS and LASSI. Moreover, it can be verified that a large number of artifacts are present in the temporal cross section produced by LASSI. On the contrary, BiLMDM provides a temporal cross-section very close to the gold standard.

## V. CONCLUSIONS

This paper proposed the novel bi-linear modeling for data manifolds (BiLMDM); a new framework for data reconstruction using manifold-learning and sparse-approximation arguments. BiLMDM comprises several modules: Extracting a set of landmark points from a data cloud helps in learning the latent manifold geometry while identifying low-dimensional renditions of the landmark points facilitates efficient means for data storage and computations. Finally, a bi-linear optimization task is used to achieve data recovery. Quantitative and qualitative analyses on dynamic MRI data, described in Sec. IV, provided evidence that the proposed BiLMDM achieves improvements over state-of-the-art approaches such as PS-Sparse, MLS, LASSI and SToRM. By introducing BiLMDM, this work paves the way for devising efficient ways to utilize fewer data points for reconstruction than state-of-the-art solutions



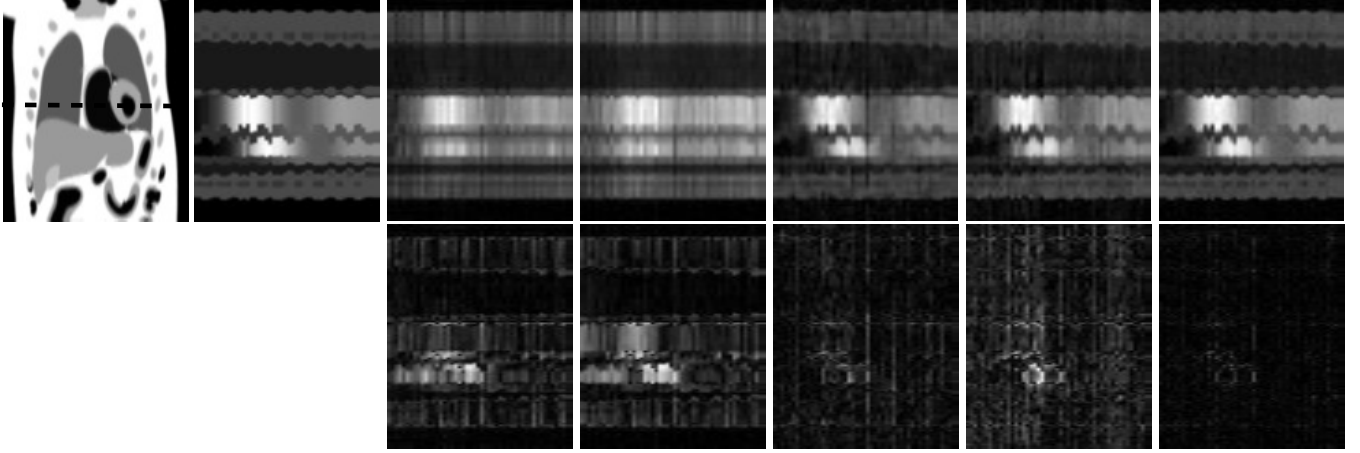


Fig. 8. Temporal cross-sections for PINCAT phantom (acceleration rate: 5x). Left to right: Gold standard (spatial frame), gold standard (temporal cross-section), PS-Sparse (0.2939), MLS (0.268), SToRM (0.2224), LASSI (0.2287) and proposed framework ( $0.1033 \pm 3.1 \times 10^{-4}$ ). The previous numerical values indicate the NRMSE for the complete dataset, in addition to the standard deviation (for the proposed scheme only) obtained after running the non-convex algorithmic scheme for 25 independent trials. Top to Bottom: Temporal cross-section and error maps. The temporal location of the frames is indicated by the dotted line in the gold-standard (spatial-frame) image.

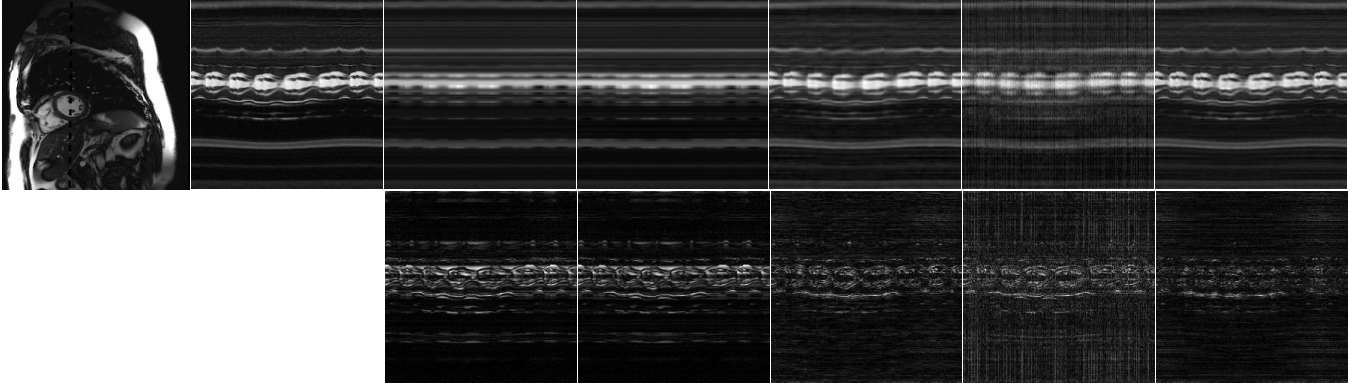


Fig. 9. Temporal cross-sections for real cardiac cine data (acceleration rate: 17x). Left to right: Gold standard (spatial frame), gold standard (temporal cross-section), PS-Sparse (0.0863), MLS (0.0892), SToRM (0.0583), LASSI (0.0791) and BiLMDM ( $0.0527 \pm 1.1 \times 10^{-4}$ ). The previous numerical values indicate the NRMSE for the complete dataset, in addition to the standard deviation (for the proposed scheme only) obtained after running the non-convex algorithmic scheme for 25 independent trials. Top to bottom: Temporal cross section and error maps. The temporal location of the frames is indicated by the dotted line in the gold-standard (spatial-frame) image.

and opens the door for further advances in geometric data-approximation methods.

#### APPENDIX A MATHEMATICAL PRELIMINARIES

For positive integers  $m, n$ , the space of matrices  $\mathbb{C}^{m \times n}$  is equipped with the inner product  $\langle \mathbf{A} | \mathbf{B} \rangle := \text{trace}(\mathbf{A}^H \mathbf{B})$ ,  $\forall \mathbf{A}, \mathbf{B} \in \mathbb{C}^{m \times n}$ , where the superscript H denotes the Hermitian transpose of a matrix. It is worth noting that the inner product is not commutative:  $\langle \mathbf{B} | \mathbf{A} \rangle = \overline{\langle \mathbf{A} | \mathbf{B} \rangle}$ , where the overline symbol denotes the complex conjugate of a number. The induced norm of  $\mathbb{C}^{m \times n}$  by the previous inner product coincides with the Frobenius norm of a matrix:  $\|\cdot\|_F = \langle \cdot | \cdot \rangle^{1/2}$ . Moreover, the spectral norm  $\|\mathbf{A}\|_2$  of matrix  $\mathbf{A} \in \mathbb{C}^{m \times n}$  is defined as  $\lambda_{\max}^{1/2}(\mathbf{A}^H \mathbf{A})$ , where  $\lambda_{\max}(\cdot)$  stands for the maximum eigenvalue of a symmetric matrix. In the case where  $m = n$ , then  $\|\mathbf{A}\|_2 = \lambda_{\max}(\mathbf{A})$ .

Given the positive integers  $m_1, m_2, n_1, n_2$  and the linear mapping  $\mathcal{L} : \mathbb{C}^{m_1 \times n_1} \rightarrow \mathbb{C}^{m_2 \times n_2}$ , the adjoint of  $\mathcal{L}$  is the linear mapping  $\mathcal{L}^* : \mathbb{C}^{m_2 \times n_2} \rightarrow \mathbb{C}^{m_1 \times n_1}$  defined as  $\langle \mathbf{A} | \mathcal{L}(\mathbf{B}) \rangle = \langle \mathcal{L}^*(\mathbf{A}) | \mathbf{B} \rangle$ ,  $\forall \mathbf{A} \in \mathbb{C}^{m_2 \times n_2}$ ,  $\forall \mathbf{B} \in \mathbb{C}^{m_1 \times n_1}$ . For example, with regards to the sampling mapping  $\mathcal{S}(\cdot)$  in Sec. III, its adjoint  $\mathcal{S}^*(\cdot) = \mathcal{S}(\cdot)$ , *i.e.*,  $\mathcal{S}(\cdot)$  is self-adjoint, and  $\mathcal{S}^2(\cdot) = \mathcal{S}(\cdot)$ . Moreover, for the MATLAB implementation of the Fourier transform [45],  $\mathcal{F}^* = N_k \mathcal{F}^{-1}$  and  $\mathcal{F}_t^* = N_{fr} \mathcal{F}_t^{-1}$ . If matrix  $\mathbf{A} \in \mathbb{C}^{m \times n}$  is viewed as a linear mapping  $\mathbf{A} : \mathbb{C}^n \rightarrow \mathbb{C}^m$ , then  $\mathbf{A}^* = \mathbf{A}^H$ . Mapping  $\mathcal{L}(\cdot)$  is called Lipschitz continuous, with coefficient  $L > 0$ , if  $\|\mathcal{L}(\mathbf{A}) - \mathcal{L}(\mathbf{B})\|_F \leq L \|\mathbf{A} - \mathbf{B}\|_F$ ,  $\forall \mathbf{A}, \mathbf{B}$ .

Given a convex function  $g(\cdot) : \mathbb{C}^{m \times n} \rightarrow \mathbb{R}$  and a positive real number  $\lambda$ , the proximal mapping  $\text{Prox}_{\lambda g}(\cdot) : \mathbb{C}^{m \times n} \rightarrow \mathbb{C}^{m \times n}$  is defined as  $\text{Prox}_{\lambda g}(\mathbf{A}) := \arg \min_{\mathbf{B}} \lambda g(\mathbf{B}) + (1/2) \|\mathbf{A} - \mathbf{B}\|_F^2$ . For example, in the case where  $g$  becomes the indicator function  $\iota_{\mathcal{C}}$  with respect to a closed convex set

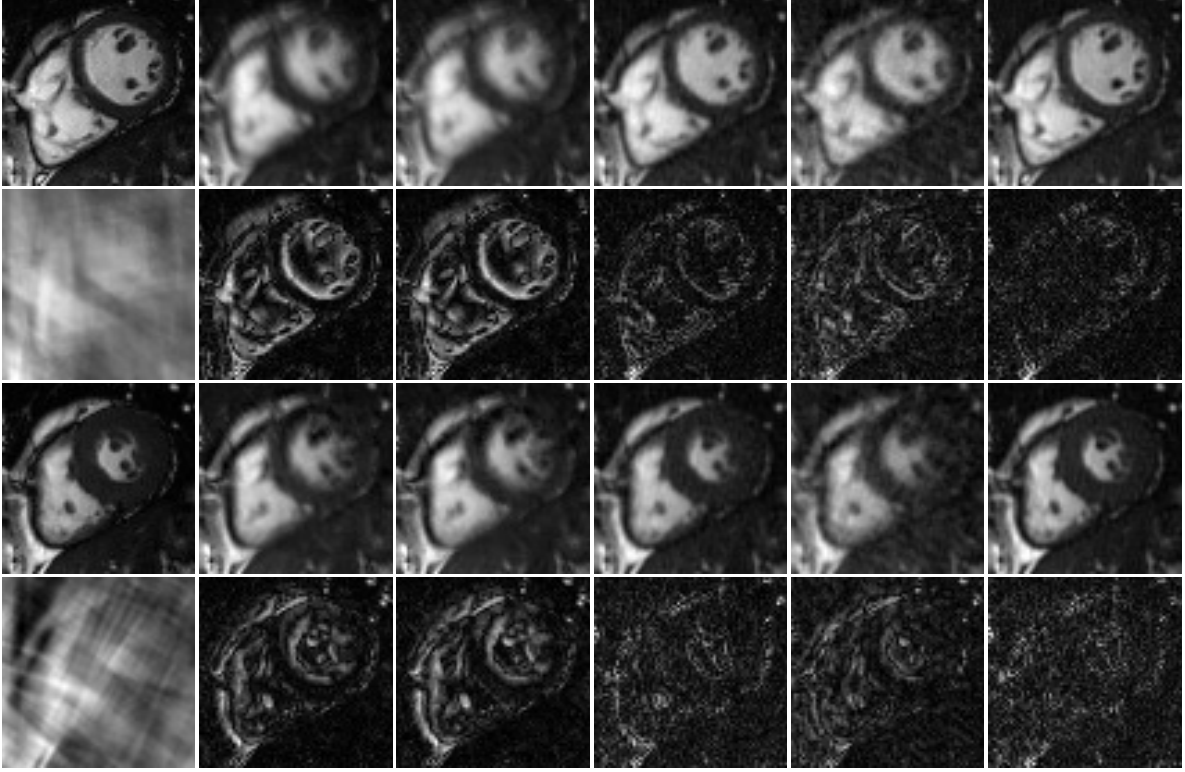


Fig. 10. Spatial results for real cardiac cine data (acceleration rate: 17x). Left to right: Gold standard, PS-Sparse (0.0863), MLS (0.0892), SToRM (0.0583), LASSI (0.0791) and BiLMDM ( $0.0527 \pm 1.1 \times 10^{-4}$ ). The previous numerical values indicate the NRMSE for the complete dataset, in addition to the standard deviation (for BiLMDM only) obtained after running the non-convex algorithmic scheme for 25 independent trials. Top to bottom: Diastole phase (frame 1 of the time series), the under-sampled image followed by error maps, systole phase (frame 16 of the time series) and the under-sampled image followed by error maps.

$\mathcal{C} \subset \mathbb{C}^{m \times n}$ , i.e.,  $\iota_{\mathcal{C}}(\mathbf{A}) := 0$ , if  $\mathbf{A} \in \mathcal{C}$ , while  $\iota_{\mathcal{C}}(\mathbf{A}) := +\infty$ , if  $\mathbf{A} \notin \mathcal{C}$ , then  $\text{Prox}_{\lambda \iota_{\mathcal{C}}}$  becomes the metric projection mapping onto  $\mathcal{C}$ :  $\text{Prox}_{\lambda \iota_{\mathcal{C}}}(\mathbf{A}) = \arg \min_{\mathbf{B} \in \mathcal{C}} \|\mathbf{A} - \mathbf{B}\|_{\text{F}}$ . Moreover, in the case where  $g$  is the  $\ell_1$ -norm  $\|\cdot\|_1$ , then the  $(i, j)$ th entry of  $\text{Prox}_{\lambda \|\cdot\|_1}(\mathbf{A})$  is given by the soft-thresholding rule [51, Lemma V.I]

$$[\text{Prox}_{\lambda \|\cdot\|_1}(\mathbf{A})]_{ij} = [\mathbf{A}]_{ij} \left( 1 - \frac{\lambda}{\max\{\lambda, |[\mathbf{A}]_{ij}|\}} \right). \quad (6)$$

#### APPENDIX B SOLVING FOR $\hat{\mathbf{U}}_n$

This refers to the convex minimization sub-task (4a) and provides important details essential to the implementation of Alg. 2. All derivations, including those in Sec. C, are performed on the basis of viewing the complex-valued  $\mathbf{U}$  as  $(\Re(\mathbf{U}), \Im(\mathbf{U}))$ , where  $\Re(\cdot)$  and  $\Im(\cdot)$  stand for the real and imaginary parts, respectively, of a complex-valued matrix. As such, gradients are *not* considered in the complex-differentiability sense (Cauchy-Riemann conditions) [52]. Nevertheless, to save space and use compact mathematical expressions, all subsequent results, including those in Sec. C, are stated in their complex-valued form.

Upon defining the convex constraint  $\mathcal{C}_i := \{\mathbf{U} \mid \|\mathbf{U}\mathbf{e}_i\| \leq C_U\}$ ,  $\forall i \in \{1, \dots, d\}$ , (4a) can be expressed as

$$\hat{\mathbf{U}}_n \in \arg \min_{\mathbf{U}} g_1(\mathbf{U}) + g_2(\mathbf{U}), \quad (7)$$

where

$$g_1(\mathbf{U}) := \frac{1}{2} \|\mathcal{S}(\mathbf{Y}) - \mathcal{S}\mathcal{F}(\mathbf{U}\check{\mathbf{A}}\mathbf{B}_n)\|_{\text{F}}^2 + \frac{\tau_U}{2} \|\mathbf{U} - \mathbf{U}_n\|_{\text{F}}^2 + \frac{\lambda_1}{2} \|\mathbf{Z}_n - \mathcal{F}_t(\mathbf{U}\check{\mathbf{A}}\mathbf{B}_n)\|_{\text{F}}^2, \quad (8)$$

$$g_2(\mathbf{U}) := \sum_{i=1}^d \iota_{\mathcal{C}_i}(\mathbf{U}). \quad (9)$$

It can be verified that  $\forall \mathbf{U}$ ,

$$\begin{aligned} \nabla g_1(\mathbf{U}) &= [N_k \mathcal{F}^{-1} \mathcal{S}\mathcal{F}(\mathbf{U}\check{\mathbf{A}}\mathbf{B}_n) + \lambda_1 N_{\text{fr}} \mathbf{U}\check{\mathbf{A}}\mathbf{B}_n] \mathbf{B}_n^H \check{\mathbf{A}}^H \\ &\quad + \tau_U (\mathbf{U} - \mathbf{U}_n) \\ &\quad - [N_k \mathcal{F}^{-1} \mathcal{S}(\mathbf{Y}) + \lambda_1 N_{\text{fr}} \mathcal{F}_t^{-1}(\mathbf{Z}_n)] \mathbf{B}_n^H \check{\mathbf{A}}^H. \end{aligned} \quad (10)$$

By virtue of the fact  $\|\mathcal{F}^{-1} \mathcal{S}\mathcal{F}(\mathbf{U})\|_{\text{F}} \leq \|\mathbf{U}\|_{\text{F}}$ ,  $\forall \mathbf{U}$ , it can be also verified that  $\forall \mathbf{U}_1, \mathbf{U}_2$ ,

$$\begin{aligned} \|\nabla g_1(\mathbf{U}_1) - \nabla g_1(\mathbf{U}_2)\|_{\text{F}} \\ \leq \|(N_k + \lambda_1 N_{\text{fr}}) \check{\mathbf{A}}\mathbf{B}_n \mathbf{B}_n^H \check{\mathbf{A}}^H + \tau_U \mathbf{I}_d\|_2 \cdot \|\mathbf{U}_1 - \mathbf{U}_2\|_{\text{F}}, \end{aligned} \quad (11)$$

which yields the Lipschitz coefficient

$$L := (N_k + \lambda_1 N_{\text{fr}}) \cdot \lambda_{\max}(\check{\mathbf{A}}\mathbf{B}_n \mathbf{B}_n^H \check{\mathbf{A}}^H) + \tau_U. \quad (12)$$

The  $i$ th column of  $\text{Prox}_{\lambda g_2}(\mathbf{U})$ ,  $\forall \lambda > 0$  and  $\forall \mathbf{U}$ , is computed by the (metric) projection mapping onto  $\mathcal{C}_i$ :

$$\text{Prox}_{\lambda g_2}(\mathbf{U})\mathbf{e}_i = \frac{C_U}{\max\{C_U, \|\mathbf{U}\mathbf{e}_i\|\}} \mathbf{U}\mathbf{e}_i. \quad (13)$$

Lastly, since (7) is not affinely constrained, [41] suggests

$$T(\mathbf{U}) = \mathbf{U}, \quad \forall \mathbf{U}, \quad (14)$$

for Alg. 2.

#### APPENDIX C SOLVING FOR $\hat{\mathbf{B}}_n$

This refers to the convex minimization sub-task (4b) and provides important details, essential to the implementation of Alg. 2. Upon defining the affine constraint  $\mathcal{C}_{\text{aff}} := \{\mathbf{B} \mid \mathbf{1}_{N_\ell}^\top \mathbf{B} = \mathbf{1}_{N_{\text{fr}}}^\top\}$ , (4b) can be expressed as

$$\hat{\mathbf{B}}_n \in \arg \min_{\mathbf{B} \in \mathcal{C}_{\text{aff}}} g_1(\mathbf{B}) + g_2(\mathbf{B}), \quad (15)$$

where

$$g_1(\mathbf{B}) = \frac{1}{2} \|\mathcal{S}(\mathbf{Y}) - \mathcal{S}\mathcal{F}(\mathbf{U}_n \check{\mathbf{A}} \mathbf{B})\|_{\text{F}}^2 + \frac{\tau_B}{2} \|\mathbf{B} - \mathbf{B}_n\|_{\text{F}}^2 + \frac{\lambda_1}{2} \|\mathbf{Z}_n - \mathcal{F}_t(\mathbf{U}_n \check{\mathbf{A}} \mathbf{B})\|_{\text{F}}^2, \quad (16)$$

$$g_2(\mathbf{B}) = \lambda_3 \|\mathbf{B}\|_1. \quad (17)$$

It can be verified that  $\forall \mathbf{B}$ ,

$$\begin{aligned} \nabla g_1(\mathbf{B}) &= \check{\mathbf{A}}^H \mathbf{U}_n^H [N_k \mathcal{F}^{-1} \mathcal{S}\mathcal{F}(\mathbf{U}_n \check{\mathbf{A}} \mathbf{B}) + \lambda_1 N_{\text{fr}} \mathbf{U}_n \check{\mathbf{A}} \mathbf{B}] \\ &\quad + \tau_B (\mathbf{B} - \mathbf{B}_n) \\ &\quad - \check{\mathbf{A}}^H \mathbf{U}_n^H [N_k \mathcal{F}^{-1} \mathcal{S}(\mathbf{Y}) + \lambda_1 N_{\text{fr}} \mathcal{F}_t^{-1}(\mathbf{Z}_n)], \end{aligned} \quad (18)$$

and by steps similar to those in Sec. B,  $\nabla g_1(\cdot)$  is Lipschitz continuous with coefficient

$$L = (N_k + \lambda_1 N_{\text{fr}}) \cdot \lambda_{\max}(\check{\mathbf{A}}^H \mathbf{U}_n^H \mathbf{U}_n \check{\mathbf{A}}) + \tau_B. \quad (19)$$

According to (6),  $\text{Prox}_{\lambda g_2}(\cdot)$  becomes:  $\forall \mathbf{B}$ ,

$$[\text{Prox}_{\lambda g_2}]_{ij} = [\mathbf{B}]_{ij} \left(1 - \frac{\lambda \lambda_3}{\max\{\lambda \lambda_3, |[\mathbf{B}]_{ij}|\}}\right). \quad (20)$$

Moreover, according to [41], mapping  $T(\cdot)$ , used in Alg. 2, is set equal to the projection mapping onto  $\mathcal{C}_{\text{aff}}$ :  $\forall \mathbf{B}$ ,

$$T(\mathbf{B}) = \mathbf{B} - \frac{1}{N_\ell} \mathbf{1}_{N_\ell} (\mathbf{1}_{N_\ell}^\top \mathbf{B} - \mathbf{1}_{N_{\text{fr}}}^\top). \quad (21)$$

#### REFERENCES

- [1] Z.-P. Liang and P. C. Lauterbur, *Principles of Magnetic Resonance Imaging: A Signal Processing Perspective*. IEEE Press, 2000.
- [2] D. E. Dudgeon and R. M. Mersereau, *Multidimensional Digital Signal Processing*. Prentice-Hall, 1984.
- [3] D. P. Petersen and D. Middleton, "Sampling and reconstruction of wave-number-limited functions in N-dimensional Euclidean spaces," *Information and Control*, vol. 5, no. 4, pp. 279–323, 1962.
- [4] Z.-P. Liang and P. C. Lauterbur, "An efficient method for dynamic magnetic resonance imaging," *IEEE Trans. Medical Imag.*, vol. 13, no. 4, pp. 677–686, 1994.
- [5] S. Wang, Z. Su, L. Ying, X. Peng, S. Zhu, F. Liang, D. Feng, and D. Liang, "Accelerating magnetic resonance imaging via deep learning," in *Proc. ISBI*, 2016, pp. 514–517.
- [6] H. Chen, Y. Zhang, M. K. Kalra, F. Lin, Y. Chen, P. Liao, J. Zhou, and G. Wang, "Low-dose CT with a residual encoder-decoder convolutional neural network," *IEEE Trans. Medical Imag.*, vol. 36, no. 12, pp. 2524–2535, 2017.
- [7] B. Zhu, J. Z. Liu, S. F. Cauley, B. R. Rosen, and M. S. Rosen, "Image reconstruction by domain-transform manifold learning," *Nature*, vol. 555, no. 7697, p. 487, 2018.
- [8] K. Hammernik, T. Klatzer, E. Kobler, M. P. Recht, D. K. Sodickson, T. Pock, and F. Knoll, "Learning a variational network for reconstruction of accelerated MRI data," *Magnetic Resonance in Medicine*, vol. 79, no. 6, pp. 3055–3071, 2018.
- [9] M. Mardani, E. Gong, J. Y. Cheng, J. Pauly, and L. Xing, "Recurrent generative adversarial neural networks for compressive imaging," in *Proc. IEEE CAMSAP*, 2017, pp. 1–5.
- [10] M. Mardani, E. Gong, J. Y. Cheng, S. Vasanawala, G. Zaharchuk, M. Alley, N. Thakur, S. Han, W. Dally, J. M. Pauly *et al.*, "Deep generative adversarial networks for compressed sensing automates MRI," *arXiv e-print*, 2017, 1706.00051.
- [11] M. Lustig, J. M. Santos, D. L. Donoho, and J. M. Pauly, "k-t SPARSE: High frame rate dynamic MRI exploiting spatio-temporal sparsity," in *Proc. ISMRM*, vol. 2420, 2006.
- [12] H. Jung, J. C. Ye, and E. Y. Kim, "Improved k-t BLAST and k-t SENSE using FOCUSS," *Physics in Medicine and Biology*, vol. 52, no. 11, pp. 3201–3226, 2007.
- [13] R. Otazo, D. Kim, L. Axel, and D. K. Sodickson, "Combination of compressed sensing and parallel imaging for highly accelerated perfusion MRI," *Magnetic Resonance in Medicine*, vol. 64, no. 3, pp. 767–776, 2010.
- [14] D. Liang, E. V. R. DiBella, R.-R. Chen, and L. Ying, "k-t ISD: Dynamic cardiac MR imaging using compressed sensing with iterative support detection," *Magnetic Resonance in Medicine*, vol. 68, no. 1, pp. 41–53, 2012.
- [15] S. G. Lingala, Y. Hu, E. V. R. DiBella, and M. Jacob, "Accelerated dynamic MRI exploiting sparsity and low-rank structure: k-t SLR," *IEEE Trans. Medical Imag.*, vol. 30, no. 5, pp. 1042–1054, 2011.
- [16] B. Zhao, J. P. Haldar, A. G. Christodoulou, and Z.-P. Liang, "Image reconstruction from highly undersampled (k,t)-space data with joint partial separability and sparsity constraints," *IEEE Trans. Medical Imag.*, vol. 31, no. 9, pp. 1809–1820, 2012.
- [17] K. T. Block, M. Uecker, and J. Frahm, "Undersampled radial MRI with multiple coils: Iterative image reconstruction using a total variation constraint," *Magnetic Resonance in Medicine*, vol. 57, no. 6, pp. 1086–1098, 2007.
- [18] F. Knoll, K. Bredies, T. Pock, and R. Stollberger, "Second order total generalized variation (TGV) for MRI," *Magnetic Resonance in Medicine*, vol. 65, no. 2, pp. 480–491, 2011.
- [19] L. Feng, R. Grimm, K. T. Block, H. Chandarana, S. Kim, J. Xu, L. Axel, D. K. Sodickson, and R. Otazo, "Golden-angle radial sparse parallel mri: combination of compressed sensing, parallel imaging, and golden-angle radial sampling for fast and flexible dynamic volumetric mri," *Magnetic Resonance in Medicine*, vol. 72, no. 3, pp. 707–717, 2014.
- [20] S. Poddar and M. Jacob, "Dynamic MRI using smoothness regularization on manifolds (SToRM)," *IEEE Trans. Medical Imag.*, vol. 35, no. 4, pp. 1106–1115, 2016.
- [21] S. Ravishanker, B. E. Moore, R. R. Nadakuditi, and J. A. Fessler, "Low-rank and adaptive sparse signal (LASSI) models for highly accelerated dynamic imaging," *IEEE Trans. Medical Imag.*, vol. 36, no. 5, pp. 1116–1128, 2017.
- [22] S. P. Awate and E. V. R. DiBella, "Spatiotemporal dictionary learning for undersampled dynamic MRI reconstruction via joint frame-based and dictionary-based sparsity," in *Proc. ISBI*, 2012, pp. 318–321.
- [23] Y. Wang and L. Ying, "Compressed sensing dynamic cardiac cine mri using learned spatiotemporal dictionary," *IEEE Trans. Biomed. Engineering*, vol. 61, no. 4, pp. 1109–1120, 2014.
- [24] J. Caballero, A. N. Price, D. Rueckert, and J. V. Hajnal, "Dictionary learning and time sparsity for dynamic MR data reconstruction," *IEEE Trans. Medical Imag.*, vol. 33, no. 4, pp. 979–994, 2014.
- [25] U. Nakarmi, Y. Zhou, J. Lyu, K. Slavakis, and L. Ying, "Accelerating dynamic magnetic resonance imaging by nonlinear sparse coding," in *Proc. ISBI*, 2016.
- [26] Y. Wang, N. Cao, Z. Liu, and Y. Zhang, "Real-time dynamic MRI using parallel dictionary learning and dynamic total variation," *Neurocomputing*, vol. 238, pp. 410–419, 2017.
- [27] U. Nakarmi, K. Slavakis, J. Lyu, and L. Ying, "M-MRI: A manifold-based framework to highly accelerated dynamic magnetic resonance imaging," in *Proc. ISBI*, 2017, pp. 19–22.
- [28] M. Usman, D. Atkinson, C. Kolbitsch, T. Schaeffter, and C. Prieto, "Manifold learning based ECG-free free-breathing cardiac CINE MRI," *J. Magnetic Resonance Imag.*, vol. 41, no. 6, pp. 1521–1527, 2015.
- [29] U. Nakarmi, K. Slavakis, and L. Ying, "MLS: Joint manifold-learning and sparsity-aware framework for highly accelerated dynamic magnetic resonance imaging," in *Proc. ISBI*, 2018, pp. 1213–1216.
- [30] Y. Shen, P. A. Traganitis, and G. B. Giannakis, "Nonlinear dimensionality reduction on graphs," in *Proc. IEEE CAMSAP*, 2017.
- [31] J. Silva, J. Marques, and J. Lemos, "Selecting landmark points for sparse manifold learning," in *Proc. NIPS*, 2006, pp. 1241–1248.

- [32] Y. Chen, M. Crawford, and J. Ghosh, "Improved nonlinear manifold learning for land cover classification via intelligent landmark selection," in *Proc. IEEE IGARSS*, 2006, pp. 545–548.
- [33] V. De Silva and J. B. Tenenbaum, "Sparse multidimensional scaling using landmark points," Stanford University, Tech. Rep., 2004.
- [34] L. W. Tu, *An Introduction to Manifolds*. New York: Springer, 2008.
- [35] K. Slavakis, G. B. Giannakis, and G. Leus, "Robust sparse embedding and reconstruction via dictionary learning," in *Proc. CISS*, Baltimore: USA, Mar. 2013.
- [36] K. Slavakis, G. N. Shetty, A. Bose, U. Nakarmi, and L. Ying, "Bilinear modeling of manifold-data geometry for dynamic-MRI recovery," in *Proc. IEEE CAMSAP*, 2017.
- [37] J. Friedman, T. Hastie, and R. Tibshirani, *The Elements of Statistical Learning*, 2nd ed. Springer, 2009.
- [38] L. K. Saul and S. T. Roweis, "Think globally, fit locally: Unsupervised learning of low dimensional manifolds," *J. Machine Learning Research*, vol. 4, pp. 119–155, 2003.
- [39] R. T. Rockafellar, *Convex Analysis*. Princeton, NJ: Princeton University Press, 1970.
- [40] E. Elhamifar and R. Vidal, "Sparse manifold clustering and embedding," in *Proc. NIPS*, Granada: Spain, Dec. 2011.
- [41] K. Slavakis and I. Yamada, "Fejér-monotone hybrid steepest descent method for affinely constrained and composite convex minimization tasks," *Optimization*, 2018, DOI: 10.1080/02331934.2018.1505885.
- [42] F. Facchinei, G. Scutari, and S. Sagratella, "Parallel selective algorithms for nonconvex big data optimization," *IEEE Trans. Signal Process.*, vol. 63, no. 7, pp. 1874–1889, 2015.
- [43] E. J. Candes, C. A. Sing-Long, and J. D. Trzasko, "Unbiased risk estimates for singular value thresholding and spectral estimators," *IEEE Trans. Signal Process.*, vol. 61, no. 19, pp. 4643–4657, 2013.
- [44] L. Wissmann, C. Santelli, W. P. Segars, and S. Kozierke, "MRXCAT: Realistic numerical phantoms for cardiovascular magnetic resonance," *Journal of Cardiovascular Magnetic Resonance*, vol. 16, no. 1, p. 63, 2014.
- [45] "MATLAB (R2018b)," The Mathworks, Inc., Natick, Massachusetts, 2018.
- [46] S. Poddar and M. Jacob, "SToRM MATLAB Package," accessed in 2018. [Online]. Available: <https://github.com/sunrita-poddar/l2SToRM>
- [47] S. Ravishankar, B. E. Moore, R. R. Nadakuditi, and J. A. Fessler, "LASSI MATLAB Package," accessed in 2018. [Online]. Available: <https://web.eecs.umich.edu/~fessler/irt/reproduce/17/ravishankar-17-lra/>
- [48] B. Sharif and Y. Bresler, "Physiologically improved NCAT phantom (PINCAT) enables in-silico study of the effects of beat-to-beat variability on cardiac MR," in *Proc. ISMRM*, vol. 3418, 2007.
- [49] S. G. Lingala, Y. Hu, E. V. R. DiBella, and M. Jacob, "k-t SLR MATLAB Package," accessed in 2018. [Online]. Available: [http://user.engineering.uiowa.edu/~jcb/software/ktslr\\_matlab/Software.html](http://user.engineering.uiowa.edu/~jcb/software/ktslr_matlab/Software.html)
- [50] Y.-C. Tsai, H.-D. Lin, Y.-C. Hu, C.-L. Yu, and K.-P. Lin, "Thin-plate spline technique for medical image deformation," *J. Medical and Biological Eng.*, vol. 20, no. 4, pp. 203–210, 2000.
- [51] A. Maleki, L. Anitori, Z. Yang, and R. G. Baraniuk, "Asymptotic analysis of complex LASSO via complex approximate message passing (CAMP)," *IEEE Trans. Information Theory*, vol. 59, no. 7, pp. 4290–4308, 2013.
- [52] S. Lang, *Complex Analysis*, 4th ed. New York: Springer, 1999.